TU Delft

Delft University of Technology

A finite element model for high enthalpy two-phase flow in geothermal wellbores

Akbar, S.; Fathianpour, N.; Al Khoury, R.

DOI
10.1016/j.renene.2016.03.034

Publication date
2016

Document Version
Accepted author manuscript

Published in
Renewable Energy

Citation (APA)
Akbar, S., Fathianpour, N., & Al Khoury, R. (2016). A finite element model for high enthalpy two-phase flow in geothermal wellbores. *Renewable Energy*, *94*, 223-236. https://doi.org/10.1016/j.renene.2016.03.034

Important note
To cite this publication, please use the final published version (if applicable).
Please check the document version above.

Copyright
Other than for strictly personal use, it is not permitted to download, forward or distribute the text or part of it, without the consent of the author(s) and/or copyright holder(s), unless the work is under an open content license such as Creative Commons.

Takedown policy
Please contact us and provide details if you believe this document breaches copyrights.
We will remove access to the work immediately and investigate your claim.

This work is downloaded from Delft University of Technology.
For technical reasons the number of authors shown on this cover page is limited to a maximum of 10.

© 2018 Manuscript version made available under CC-BY-NC-ND 4.0 license
https://creativecommons.org/licenses/by-nc-nd/4.0/

A finite element model for high enthalpy two-phase flow in geothermal wellbores

S. Akbar[1,2,*], N. Fathianpour[1], R. Al Khoury[2]

[1] Faculty of mining Engineering, Isfahan University of technology, PO Box 8415683111, Isfahan, Iran.

[2] Faculty of Civil Engineering and Geosciences, Delft University of Technology, PO Box 5048, 2600 GA Delft, the Netherlands

[*] Corresponding author: Tel.: +31 644338941. E-mail address: sa.3761@gmail.com (S. Akbar).

Abstract

This paper introduces a computational model for transient high enthalpy fluid flow through geothermal wellbores. The drift-flux model is utilized to formulate the physical behavior of fluid, and the constitutive relationships are described using relevant equations of state and empirical relationships. The governing equations are solved using the finite element method. All important physical phenomena and processes occurring along the wellbore, including buoyancy, phase change, compressibility, thermal interaction, wall friction and slip between phases are considered. Airlifting of water and air, initially existing in the wellbore before production, is also considered. During airlifting and early stages of production, two fluids exist along the wellbore: airlifted water-dry air fluid, and reservoir water-vapor fluid; giving rise to a discontinuity in thermodynamic properties between the two fluids. The discontinuity is modeled using the level-set method. Two numerical examples illustrating the computational capability and accuracy of the model are presented. The physical phenomena occurring during airlifting and production along the wellbore are highlighted.

Keywords: High enthalpy geothermal systems, wellbore, drift-flux model, level set, airlift.

1 Introduction

With the growing demand of renewable energy and the associated growth of interest and investment in geothermal energy extraction, the development of computational models for the simulation of a wide range of geothermal systems is inevitable. Predicting the fluid properties along the wellbore, such as temperature, phase composition and mass density is vital for the design and monitoring of geothermal systems. This constitutes the main objective of this research work, which aims at the development of a computational tool for deep high enthalpy geothermal systems consisting of multilevel geothermal reservoirs operated by multiple wellbores.

In deep high enthalpy geothermal systems, the fluid along the wellbore exhibits phase change, manifested by flash evaporation due to pressure reduction accompanied by a certain range of temperature. Below the flash evaporation point, in the upstream, the fluid is liquid, while immediately above it, the fluid is a mixture of water liquid and vapor. This sudden change in

material composition can cause significant change in its properties and behavior. Such kind of physical behavior is computationally challenging and demanding. It requires innovative conceptual modeling, descriptive mathematical formulation and robust numerical discretization.

Several geothermal models and simulators are available in literature. Pioneering works have been introduced by Poettmann and Carpenter (1952), Zuber and Findlay (1965) and Gould (1974), who simulated steady-state heat and fluid flow in wellbores with two separated phases with slip between them [1-3]. Miller (1980) was one of the first to developed a transient wellbore simulator, WELBORE [4, 5]. Bjornsson and Bodvarsson (1987) stimulated one and two phase flow along a vertical wellbore with multiple feed zones, and developed HOLA code, which later on expanded to handle CO2-H2O and NaCl-H2O systems [6, 7]. Gudmundsdottir et al. (2013) developed a steady state model for one and two sliding separated phase flow along a wellbore, and compared their results with measured data and existing models [8]. These models, and most of existing simulators, are based on the finite difference or finite volume methods. On the other hand, Saeid et al. (2013) introduced a finite element model for low enthalpy deep geothermal systems [9].

Here, we solve the heat and fluid flow in a high enthalpy deep geothermal wellbore using the finite element method. We utilize the drift-flux model [10-13] to simulate transient heat flow of a compressible, two-phase fluid travelling along the wellbore. This model adopts the area-averaged approach, where detailed analysis of the local behavior of the involved phases are averaged over the cross-sectional area of the wellbore [14]. All important physical phenomena and processes occurring along the wellbore, including fluid dynamics, buoyancy, phase change, compressibility, thermal interaction, wall friction and slip between phases are considered. Airlifting of water and air, initially existing in the wellbore before production, is also considered. Airlifting is a process to facilitate fluid production by injecting air into an existing fluid to reduce its mass density. During early stages of production, two fluids exist along the wellbore: the wellbore airlifted water-dry air fluid, and the reservoir water-vapor fluid. This process inevitably generates an interface between the two fluids that exhibits a jump in mass density, specific enthalpy and other thermodynamic properties. The jump is modeled here using the level-set method [15, 16], and coupled to the drift-flux model.

Numerical discretization of the mathematical model and implementation are conducted using the finite element package COMSOL Multiphysics. As the model is compressible, highly advective, non-linear and involves forces with opposite effects, such as buoyance that tempts to force the fluid to flow against gravity, and drag forces that temp to impede the buoyance, it is not possible to use the standard strong form implementation of the partial differential equations in COMSOL. Instead, the weak form is implemented.

In this paper, we introduce a detailed formulation of the governing balance equations and their relevant constitutive equations and equations of state. A detailed weak form formulation of the governing partial differential equations, tailored for implementation in COMSOL, is also

introduced. We discuss the capability of the model to simulate heat and fluid flow in a vertical wellbore, which might be embedded in a wide range of high enthalpy reservoirs. Comparison to field data is also introduced.

2 Mathematical model formulation

The drift-flux model is utilized to formulate heat and fluid flow of a compressible two-phase mixture along a one-dimensional wellbore subjected to pumping at its upper boundary. Important aspects of fluid dynamics such as the inertia force, buoyancy, wall friction, drift velocity, flow profile, together with the jump in thermodynamic properties between the airlifted mixture and the reservoir mixture, are considered.

2.1 Balance equations

Using the drift-flux model, the transient fluid flow in a one-dimensional wellbore with a constant cross-sectional area can be described as

Mass balance

$$\frac{\partial \rho_m}{\partial t} + \frac{\partial \rho_m u_m}{\partial z} = 0 \quad (1)$$

Momentum balance

$$\frac{\partial \rho_m u_m}{\partial t} + \frac{\partial}{\partial z}(\rho_m u_m^2 + \gamma) = -\frac{\partial P}{\partial z} - \frac{f \rho_m |u_m| u_m}{4 r_i} - \rho_m \, g \, sin\theta \quad (2)$$

Energy balance

$$\frac{\partial}{\partial t}\left[\left(\rho_m h_m + \frac{\rho_m u_m^2}{2}\right) - P\right] + \frac{\partial}{\partial z}\left[\rho_m u_m \left(h_m + \frac{u_m^2}{2}\right)\right] = \frac{Q(z)}{\pi r_i^2} - \rho_m u_m \, g \, sin\theta \quad (3)$$

where r_i is the inner radius of the wellbore, ρ_m is the fluid mixture density, u_m is the mixture velocity, P is the pressure, g is the gravitational constant, θ is the inclination angle of the wellbore, h_m is the specific enthalpy of the mixture, f is the wall friction coefficient, Q is the heat exchange between the wellbore and its surrounding formation, and γ is the slip between phases. Detailed formulation of f, Q and γ are given in Appendix A.

In hydrothermal high enthalpy systems, the thermodynamic state quantities, given in Eqs. (1)-(3), play a major role in the fluid flow along the wellbore. The coupling between the fluid mass density, pressure, enthalpy, temperature and velocity significantly affect the mass and volume flow rates along the wellbore and, hence, the amount of energy production, which constitutes the main objectives of constructing geothermal energy systems. As the mass density and temperature are functions of pressure and specific enthalpy, and as the fluid velocity is important in determining the mass flow rate, we select the mixture pressure, P, specific enthalpy, h_m, and velocity, u_m, as the primary state variables. They are explicitly determined from solving the balance equations, Eqs. (1)-(3). The mass density and temperature are determined from the primary state variables via their equations of state and other relevant empirical relationships.

2.2 Constitutive equations

Physical characteristics of the formation water play a significant role on the flow along the wellbore, and their good characterization is essential for the accuracy of computational results. The mass density, in particular, plays a major role in determining the pressure and temperature distribution along the wellbore, and together with the wall friction, slip between phases, and thermal interaction with surrounding rock formation determine the mass and volume flow rates.

The formation water mass density is a function of pressure, temperature, vapor volume fraction and the type and amount of dissolved saline minerals and gases. The proposed model is generic and can be tailored to a wide range of pressure and enthalpy, but for the current research work, the focus is placed on the specific enthalpy range between 900 $(kJ\ kg^{-1})$ and 1100 $(kJ\ kg^{-1})$, and pressure range between 1 *bar* and 117 *bar*. In these ranges, for low saline reservoirs, the salinity effect is not significant [17, 18], and accordingly, the properties of the formation water can be described in terms of the equations of state of pure water. The formation water is assumed a mixture of two phases: liquid water and vapor, which, depending on the temperature and pressure, a single phase or both phases can exist in space.

Mixture mass density

The two-phase water mixture density is described as

$$\rho_m = \alpha\rho_g + (1-\alpha)\rho_l \quad (4)$$

in which α is the vapor volume fraction, and ρ_g and ρ_l are the gas and liquid phase densities, respectively, defined as

$$\rho_l(P,T) = 1/\left(\frac{\partial g_1}{\partial P}\right)_T \quad (5)$$

$$\rho_g(P,T) = 1/\left(\frac{\partial g_2}{\partial P}\right)_T \quad (6)$$

where g_1 and g_2 are the specific Gibbs free energy of the liquid and gas phases, respectively, given in Appendix B.

The void fraction determines the volume occupied by vapor, making it an important parameter in predicting the pressure drop along the wellbore. Rouhani and Axelsson (1970) proposed a semi-empirical void fraction formulation, which is a function of vapor mass fraction, phases densities and mass velocity, given as [19, 20]:

$$\alpha = \frac{X\,\rho_l}{C_0 X\,\rho_l + C_0(1-X)\rho_g + \dfrac{\rho_g\rho_l u_{gu}}{\rho_m u_m}} \quad (7)$$

where C_0 is the profile parameter, and u_{gu} is the drift flux velocity, given in details in Appendix A. X is the vapor mass fraction, also known as the vapor quality, defined as

$$X = \frac{h_m - h_l}{h_g - h_l} \quad (8)$$

where h_l and h_g are the enthalpies of the liquid and gas phases, respectively, defined as:

$$h_l(P,T) = g_1 - T\left(\frac{\partial g_1}{\partial T}\right)_P \quad (9)$$

$$h_g(P,T) = g_2 - T\left(\frac{\partial g_2}{\partial T}\right)_P \quad (10)$$

in which T is the temperature.

Mixture temperature

The mixture temperature distribution along the wellbore is considerably affected by the reservoir pressure and enthalpy. Reservoirs at different regions exhibit different ranges of pressure and enthalpy. Figure 1 shows the pressure-temperature and the pressure-specific enthalpy properties of pure water. They are described by four main regions, with region 2 divided into three sub-regions. The regions are defined by the equations of state provided by the International Association for the Properties of Water and Steam (IAPWS). Here, the interest is on enthalpy and pressure ranges that generate liquid water, vapor and a mixture of them, namely, Regions 1, 2 and 4 in Figure 1.

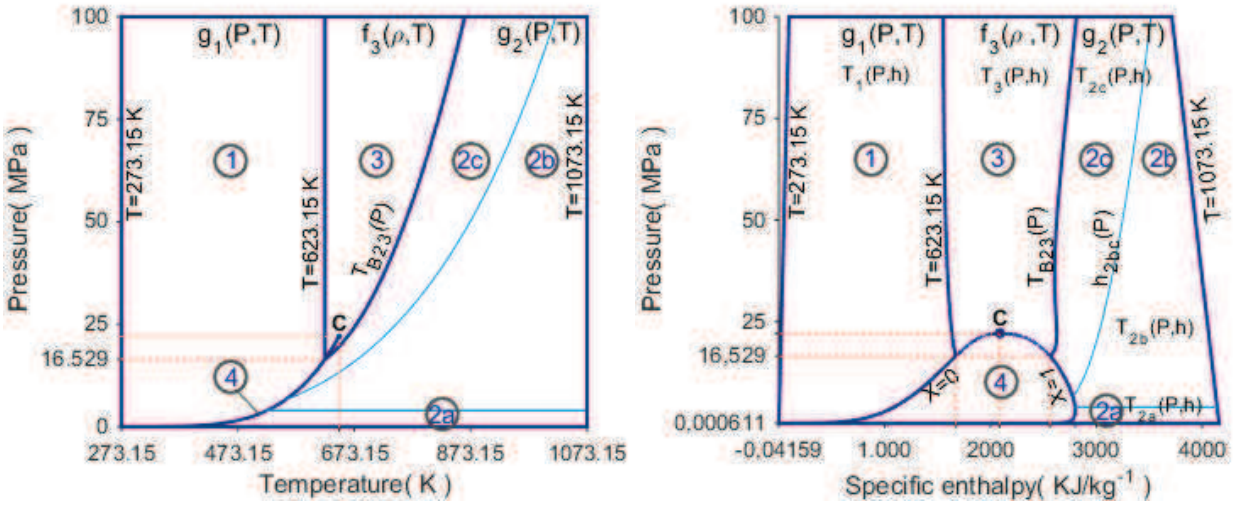

Figure 1: Pressure-temperature and pressure-specific enthalpy relationships of pure water, adopted from IAPWS-IF97 [21]

According to Figure 1, the temperature is calculated using the following algorithm:

$$\begin{aligned}
&\text{if } P \le 16.529\text{E}6 \\
&\quad \text{if } h_m \le h_l(P, T_s(P)) \text{ then } T = T_1 \\
&\quad\quad \text{elseif } h_m \le h_g(P, T_s(P)) \text{ then } T = T_s \\
&\quad\quad\quad \text{elseif } P \le 4 \text{ then } T = T_{2a} \\
&\quad\quad\quad\quad \text{elseif } h_m \le h_{2bc}(P) \text{ then } T = T_{2c} \\
&\quad\quad\quad\quad\quad \text{else } T = T_{2b}
\end{aligned} \quad (11)$$

end
end
end
end
elseif $h_m \le h_l(P, 623.15)$ then $T = T_1$
else if $h_m \ge h_g\left(P, T_{B23}(P)\right)$
if $h_m \le h_{2bc}(P)$ then $T = T_{2c}$
else $T = T_{2b}$
end
else if $P \le P_{s3}(h)$ then $T = T_s$
else $T = T_3$
end
end
end

where the temperature is in Kelvin, P in Pa and h_m in $J\,kg^{-1}$. In Eq. (11), h_l and h_g are described in Eqs. (9) and (10), respectively; T_1 is the liquid temperature, given by

$$T_1(P, h_m) = \sum_{i=1}^{20} n_i \left(\frac{P}{1\text{E}6}\right)^{I_i} \left(\frac{h_m}{2.5\text{E}6} + 1\right)^{J_i} \quad (12)$$

T_{2a}, T_{2b} and T_{2c} are the gas phase temperature in sub-regions 2a, 2b and 2c (Figure 1), given, respectively, by

$$T_{2a}(P, h_m) = \sum_{i=1}^{34} n_i \left(\frac{P}{1\text{E}6}\right)^{I_i} \left(\frac{h_m}{2\text{E}6} - 2.1\right)^{I_i} \quad (13)$$

$$T_{2b}(P, h_m) = \sum_{i=1}^{38} n_i \left(\frac{P}{1\text{E}6} - 2\right)^{I_i} \left(\frac{h_m}{2\text{E}6} - 2.6\right)^{I_i} \quad (14)$$

$$T_{2c}(P, h_m) = \sum_{i=1}^{23} n_i \left(\frac{P}{1\text{E}6} + 25\right)^{I_i} \left(\frac{h_m}{2\text{E}6} - 1.8\right)^{I_i} \quad (15)$$

T_s is the saturation temperature, a function of saturation pressure P_s, belongs to the two-phase zone, region 4 (Figure 1), given by the quadratic equation [21]:

$$\begin{aligned} & P_s^{0.5}\left(T_s + \frac{n_9}{T_s - n_{10}}\right)^2 + n_1 P_s^{0.5}\left(T_s + \frac{n_9}{T_s - n_{10}}\right) + n_2 P_s^{0.5} \\ & \quad + n_3 P_s^{0.25}\left(T_s + \frac{n_9}{T_s - n_{10}}\right)^2 + n_4 P_s^{0.25}\left(T_s + \frac{n_9}{T_s - n_{10}}\right) \\ & \quad + n_5 P_s^{0.25} + n_6\left(T_s + \frac{n_9}{T_s - n_{10}}\right)^2 + n_7\left(T_s + \frac{n_9}{T_s - n_{10}}\right) + n_8 \\ & \quad = 0 \end{aligned} \quad (16)$$

T_3 is the water temperature in region 3 (Figure 1). The temperature in this region is more than 350 °C, which is beyond the scope of the applications in this work.

T_{B23} is the water temperature at the boundary line between region 2 and region 3 in Figure 1, defined as

$$T_{B23}(P) = n_4 + \left[\left(\frac{P}{1\text{E}6} - n_5\right)/n_3\right]^{0.5} \quad (17)$$

h_{2bc} is the specific enthalpy of the cross-border of region 2, given by

$$h_{2bc}(P) = 1000(n'_4 + \left[\left(\frac{P}{1\text{E}6} - n'_5\right)/n'_3\right]^{0.5}) \quad (18)$$

and P_{s3} is the pressure at the boundary line between region 3 and region 4, given by

$$P_{s,3}(h_m) = \sum_{i=1}^{14} 22 * 10^6 * n_i \left(\frac{h_m}{2.6\text{E}6} - 1.02\right)^{I_i} \left(\frac{h_m}{2.6\text{E}6} - 0.608\right)^{J_i} \quad (19)$$

where the coefficient $n_i, n_{\text{i}}^{\text{o}}, n'_{\text{i}}, I_i, J_i, J_{\text{i}}^{\text{o}}$ can be found in IAPWS-IF97 [21].

Other constitutive relationships

Constitutive relationships for the mixture specific isobaric heat capacity (C_{p_m}), dynamic viscosity (μ_m) and thermal conductivity (λ_m) are given in Appendix A.

2.3 Initial and boundary conditions

Initially, the primary state variables might be described as

$$G(z,0) = G_0(z) \quad \text{at } t = 0 \quad (20)$$

where G could be P, u_m or h_m.

The Dirichlet boundary conditions can be described as

$$G(z,t) = \hat{G}(z,t) \quad \text{on } \Gamma \quad (21)$$

in which Γ is a boundary in the physical system.

The Neumann boundary conditions are defined as

$$\begin{aligned} \hat{q}_\rho &= (\hat{\rho}_m \hat{u}_m).\text{n} \\ \hat{q}_u &= (\hat{\rho}_m \hat{u}_m^2 + \hat{\gamma}).\text{n} \qquad \text{on } \Gamma_q \\ \hat{q}_e &= \left(\hat{\rho}_m \hat{u}_m \left(\hat{h}_m + \frac{\hat{u}_m^2}{2}\right)\right).\text{n} \end{aligned} \quad (22)$$

where Γ_q is the Neumann boundary, and the subscripts ρ, u, and e refer to the mass, momentum, and energy balance equations, respectively.

3 Numerical model formulation

The governing equations are solved using the finite element method. The finite element

179 package, COMSOL Multiphysics, is utilized as a framework for implementing and discretizing
180 the governing equations.
181 The governing drift-flux equations, Eqs. (1)-(11), together with the initial and boundary
182 conditions, Eqs.(21)-(22), form an initial and boundary value problem that is dynamic,
183 advective, nonlinear and involves phase change, together with buoyancy, friction and slip
184 forces. Solving such a problem using standard strong form implementation in COMSOL, as given
185 by the "Physics" option, entails utilization of excessively fine meshes and small time steps, but
186 yet, the calculation can be unstable and non-convergent. To tackle this, we solve the problem
187 by formulating the weak forms of the governing equations using the weighted residual finite
188 element method, and inserting them into COMSOL via the "PDE Interface".

189 **3.1 Weak form formulation**

190 Using the weighted residual finite element method, the balance equations (1), (2) and (3),
191 together with the boundary conditions , Eqs.(21)-(22), can be described as

192 **Mass balance**

$$\int_L W\left(\frac{\partial \rho_m}{\partial t}+\frac{\partial \rho_m u_m}{\partial z}\right)dz=0$$

193 where W is the weighting function and L is the element length. Solving the involved product
194 derivatives, applying the Green's function, and imposing the Neumann-boundary condition (the
195 first equation in Eq. (22)), the weak form of the mass balance equation can be described as

$$\int_L W\frac{\partial \rho_m}{\partial t}dz-\int_L \rho_m u_m\frac{\partial W}{\partial z}dz+W\hat{q}_\rho\big|_{\Gamma_q}=0 \qquad (23)$$

196 **Momentum balance**

$$\int_L W\left(\rho_m\frac{\partial u_m}{\partial t}+u_m\frac{\partial \rho_m}{\partial t}+\frac{\partial \rho_m u_m^2}{\partial z}+\frac{\partial \gamma}{\partial z}+\frac{\partial P}{\partial z}+\rho\, g\, sin\theta+\frac{f\rho_m|u_m|u_m}{4r_i}\right)dz=0 \qquad (24)$$

197 Solving the involved product derivatives, applying the Green's function, and imposing the
198 Neumann-boundary condition, the second equation of Eq. (22), the weak form of the
199 momentum balance equation can be described as
200

$$\int_L W\rho_m\frac{\partial u_m}{\partial t}dz+\int_L Wu_m\frac{\partial \rho_m}{\partial t}dz-\int_L \rho_m u_m^2\frac{\partial W}{\partial z}dz-\int_L \gamma\frac{\partial W}{\partial z}dz+W\hat{q}_u|_{\Gamma_u}+\int_L W\frac{\partial P}{\partial z}dz$$
$$+\int_L W\,\rho_m\, g\, sin\theta dz+\int_L W\frac{f\rho_m|u_m|u_m}{4r_i}dz=0$$

201 **Energy balance**

$$\int_L W\,A\left(\frac{\partial}{\partial t}\left[\left(\rho_m h_m+\frac{\rho_m u_m^2}{2}\right)-P\right]+\frac{\partial}{\partial z}\left[\rho_m\, u_m\left(h_m+\frac{u^2}{2}\right)\right]+\frac{Q}{\pi r_i^2}-\rho_m\, u_m\, g\, sin\theta\right)dz=\ 0$$

202

Solving the involved product derivatives, applying the Green's function, and imposing the Neumann-boundary condition, the third equation of Eq. (22), the weak form of the energy balance equation can be described as

$$\int_L W\rho_m \frac{\partial h_m}{\partial t} dz + \int_L W h_m \frac{\partial \rho_m}{\partial t} dz + \frac{1}{2}\int_L W u_m^2 \frac{\partial \rho_m}{\partial t} dz + \int_L W\rho_m u_m \frac{\partial u}{\partial t} dz - \int_L W \frac{\partial P}{\partial t} dz + \int_L W\rho_m u_m \frac{\partial h_m}{\partial z} dz + \int_L W h_m \frac{\partial u_m \rho_m}{\partial z} dz - \frac{1}{2}\int_L \rho_m u_m^3 \frac{\partial W}{\partial z} dz + W\hat{q}_e|_{\Gamma_e} + \int_0^L \frac{WQ}{\pi r_i^2} dz - \int_0^L W\rho_m u_m g sin\theta \, dz = 0$$

According to the mass balance equation, Eq. (23), the sum of the second term and seventh term of the energy balance equation is by definition zero, yielding

$$\int_L W\rho_m \frac{\partial h_m}{\partial t} dz + \frac{1}{2}\int_L W u_m^2 \frac{\partial \rho_m}{\partial t} dz + \int_L W\rho_m u_m \frac{\partial u}{\partial t} dz - \int_L W \frac{\partial P}{\partial t} dz + \int_L W\rho_m u_m \frac{\partial h_m}{\partial z} dz - \frac{1}{2}\int_L \rho_m u_m^3 \frac{\partial W}{\partial z} dz + W\hat{q}_e|_{\Gamma_e} + \int_L \frac{WQ}{\pi r_i^2} dz - \int_L W\rho_m u_m g sin\theta \, dz = 0 \quad (25)$$

The mass density and temperature are important state variables and several other parameters and states variables are dependent on them. It is therefore necessary to formulate them in terms of their weighted forms to make them compatible with the primary state variables and to facilitate the linearization scheme, which is internally conducted by COMSOL. Applying the weighted residual method to the void fraction equation, Eq. (7), and solving, gives

$$\int_L W'\left(X\,\rho_l\,\rho_m u_m - \alpha C_0 X\,\rho_l\,\rho_m u_m - \alpha C_0(1-X)\rho_g\rho_m u_m - \alpha\rho_g\rho_l u_{gu}\right) dz = 0 \quad (26)$$

The same can be applied to Eq. (4), giving

$$\int_L W'\left(\alpha\rho_g + (1-\alpha)\rho_l - \rho_m\right) dz = 0 \quad (27)$$

Similarly, applying the weighted residual method to the temperature equation, Eq. (11), gives

$$\int_L W'\Big(\text{if}\Big(P \le 16.529\text{E}6, \text{if}\,\big(h_m \le h_l\big(P, T_s(P)\big),\ T_1, \text{if}\,\big(h_m \le h_g\big(P, T_s(P)\big), T_s, \text{if}\big(P \le 4E6, T_{2a}, \text{if}(h_m \le h_{2bc}(P), T_{2c}, T_{2b})\big)\big)\Big), \text{if}\Big(h_m \le h_l(P, 623.15), T_1, \text{if}\Big(h_m \ge h_g\big(P, T_{B23}(P)\big), \text{if}(h_m \le h_{2bc}(P), T_{2c}, T_{2b}), \text{if}(P \le P_{s3}(h), T_s, T_3)\big)\Big)\Big) - T\Big)\,dz = 0 \quad (28)$$

in which W' is the weighting function, which can be different than that the balance equations. Formulating the constitutive equations by their weighted forms proved to be effective for solving such a problem, which exhibits advection and phase change. Otherwise, the use of the standard linearization of the constitutive equations, which is normally conducted by COMSOL, can cause numerical nuisance and divergence.

3.1.1 COMSOL Element technology and solver

COMSOL provides a wide range of element types. We utilize the Lagrange test functions for the discretization of the primary state variables. To increase accuracy and decrease oscillations, cubic shape functions are utilized for primary state variables *P*, u_m and h_m, and quadratic for temperature, mass density and void fraction.

The time-dependent fully coupled solver has been employed to solve the finite element equations, and the Backward Differentiation Formula (BDF) has been utilized for the time stepping. The nonlinear systems of equations are solved using a damped Newton method [22].

4 Numerical examples and validation

Two numerical examples are presented. The first describes the model capability to simulate heat and fluid flow in a geothermal wellbore, which can be connected to a wide range of reservoir enthalpies. The second example focuses on a high enthalpy case, which is utilized to validate the model.

4.1 Phase change in low to high enthalpy reservoirs

This example presents a numerical simulation of a production wellbore, which can be employed in various types of geothermal reservoirs ranging from low to high enthalpy. The objective of this example is to examine the capability of the computational model for the simulation of the fluid phase change along the wellbore and its association with the reservoir type. Also, it aims at gaining an insight on the physical processes and phenomena occurring along the wellbore and with time.

The wellbore geometry and its boundary conditions are shown in Figure 2. The properties of the wellbore and the surrounding formation are given in Table 1.

4.1.1 Initial and boundary conditions

Initially, the wellbore is assumed to be filled with liquid water, which is under thermal and mechanical equilibrium with the atmosphere at the top, low enthalpy reservoir at the bottom and surrounding rock formation along its length.

Due to the hydrostatic pressure and gravity force, and mass density variation with pressure and enthalpy, the thermal and mechanical equilibrium must be attended before conducting the transient analysis. For this, we conducted a steady state analysis based on the initial fluid state and boundary conditions. A constant flow rate with a constant velocity was imposed at the well head. The computational result of this analysis is utilized as the initial condition for the transient analysis.

Table 1: Wellbore and formation assumed data

Inclination Angle	90
Well inner radius (r_i)	0.11 (m)
Casing outer radius (r_o)	0.13 (m)
Length (l)	1000 (m)
Casing thermal conductivity (λ_p)	0.33 ($Wm^{-1}K^{-1}$)
Roughness of the wellbore (ε)	1.5E-6 (m)
Surface temperature $(T_{surface})$	20 °C
Profile parameter (C0) & Drift flux velocity (u_{gu})	Eq. (A 7)

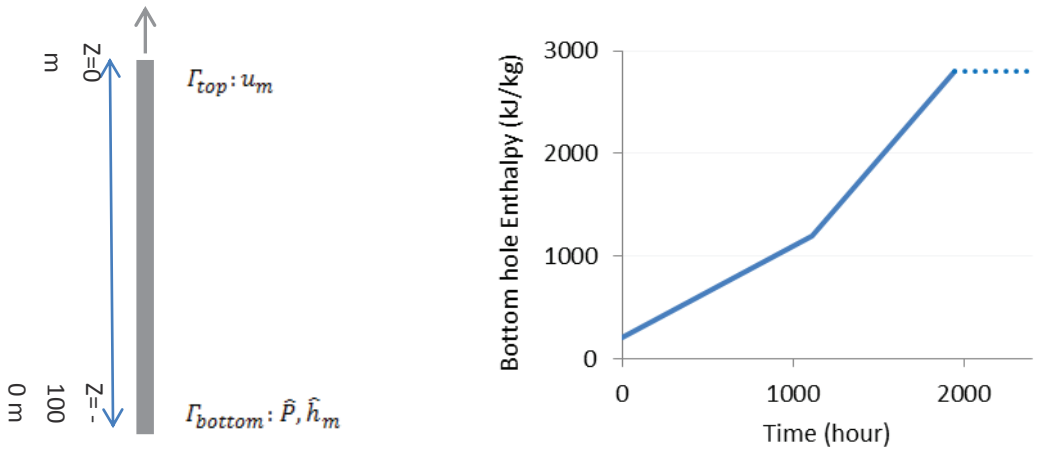

Figure 2: Geometry and the boundary conditions

The boundary conditions in the transient analysis are:

$$\hat{u}_m = 3\ m/s \quad \text{at z = 0 m}$$

$$\hat{P} = 10\ \text{MPa} \quad \text{at z = -1000 m} \qquad (29)$$

$$\hat{h}_m = \begin{cases} 0.25t + 2\text{E}5 & t \le 4\text{E}6\ s \\ 0.533t - 9.32\text{E}3 & 4\text{E}6\ s < t \le 7\text{E}6\ s \\ 2.8\text{E}6 & t \ge 7\text{E}6\ s \end{cases} \quad Jkg^{-1}K^{-1} \quad \text{at z = -1000 m}$$

where $\hat{h}_m$ variation with time is plotted in Figure 2.

These boundary conditions are chosen to simulate a wide range of geothermal reservoirs, ranging from low to high enthalpy.

The temperature of the formation rocks surrounding the wellbore, T_R , appearing in the heat exchange term, Q in Eq. (A 10), is adjusted according to the temperature at the bottom hole, which is a function of pressure and specific enthalpy as given in Eq. (29), as

$$T_R = \begin{cases} 293.15 + (T_{bottom} - 293.15) * \text{H}/1000 & T \le 523.15\ K \\ 293.15 + 0.23 * H & T > 523.15\ K \end{cases}$$

in which T_{bottom} is the bottom hole temperature, calculated at every time step; and H is the wellbore length.

4.1.2 Finite element solution and results

The weak forms given in Section 3.1 are implemented in COMSOL, and the problem is discretized using linear elements, approximately 20 m in length for each. The physical time for the wellbore production is assumed 2083 hours.

The computational results along the wellbore and with time for temperature, pressure, vapor volume fraction, vapor mass fraction, mass density and mixture velocity are given in Figure 3.

Figure 3a shows the pressure distribution along the wellbore at different times. It shows that, initially, the pressure is hydrostatic, but increasing with time due to the thermodynamic effects of varying temperature and density along the wellbore. The wellhead pressure changes from 0.6 bar, during the production of hot water at the initial stage, to about 95 bar, during the production of the high temperature vapor at the final stage. As expected, the vapor volume fraction plays an important role in the pressure drop along the wellbore.

Figure 3b shows the temperature distribution along the wellbore and with time. The temperature at the bottom varies from 45 ℃ to about 323℃. By increasing enthalpy, the flash evaporation point moves downwards until reaching to a vapor state at the bottom hole. This is apparent from Figure 3c which shows the vapor volume distribution. As the pressure at the bottom hole is constant and the temperature in the two-phase region is a function of pressure only (Eq.(16)), the bottom hole temperature keeps constant in the period between t = 1316 hour and t = 1716 hour, which is related to the specific enthalpy range between 1592 $(kJ\ kg^{-1})$ and 2360 $(kJ\ kg^{-1})$, and the void fraction between 0.51 and 0.88, respectively.

Figure 3c and Figure 3d show the vapor volume fraction and the vapor mass fraction, respectively. They vary between 0 and 1, entailing the variation of fluid state from liquid to mixture to a saturated vapor state.

The increase of the vapor content with time is accompanied with the reduction of mass density and increase in velocity, as shown in Figure 3e and Figure 3f, respectively. Velocity logs show an

292 apparently linear trend when only single phase exists along the wellbore, but exhibits a sharp
293 gradient at the flashing or condensation zones. Interesting to observe that, with vaporization
294 (the period between t =746 h and t = 1186 h), the fluid runs faster, but with condensation (the
295 period indicated at t = 2016 h) the fluid runs slower. This behavior is reflected in the mass
296 density distribution in Figure 3e, but in an inverse sense. At z = -1000 m the mass density at the
297 bottom hole changes from 994 kg/m3, in the low enthalpy liquid water state, to 51 kg/m3, in
298 the saturated vapor state. The transient changes of the mass density and the location of the
299 flash points are in accordance with the variations in the other state variables.
300 Briefly, the computational results, as illustrated in Figure 3, show the computational capability
301 of the proposed model to simulate a wide range of wellbore behaviors exhibiting rigorous
302 phase change.

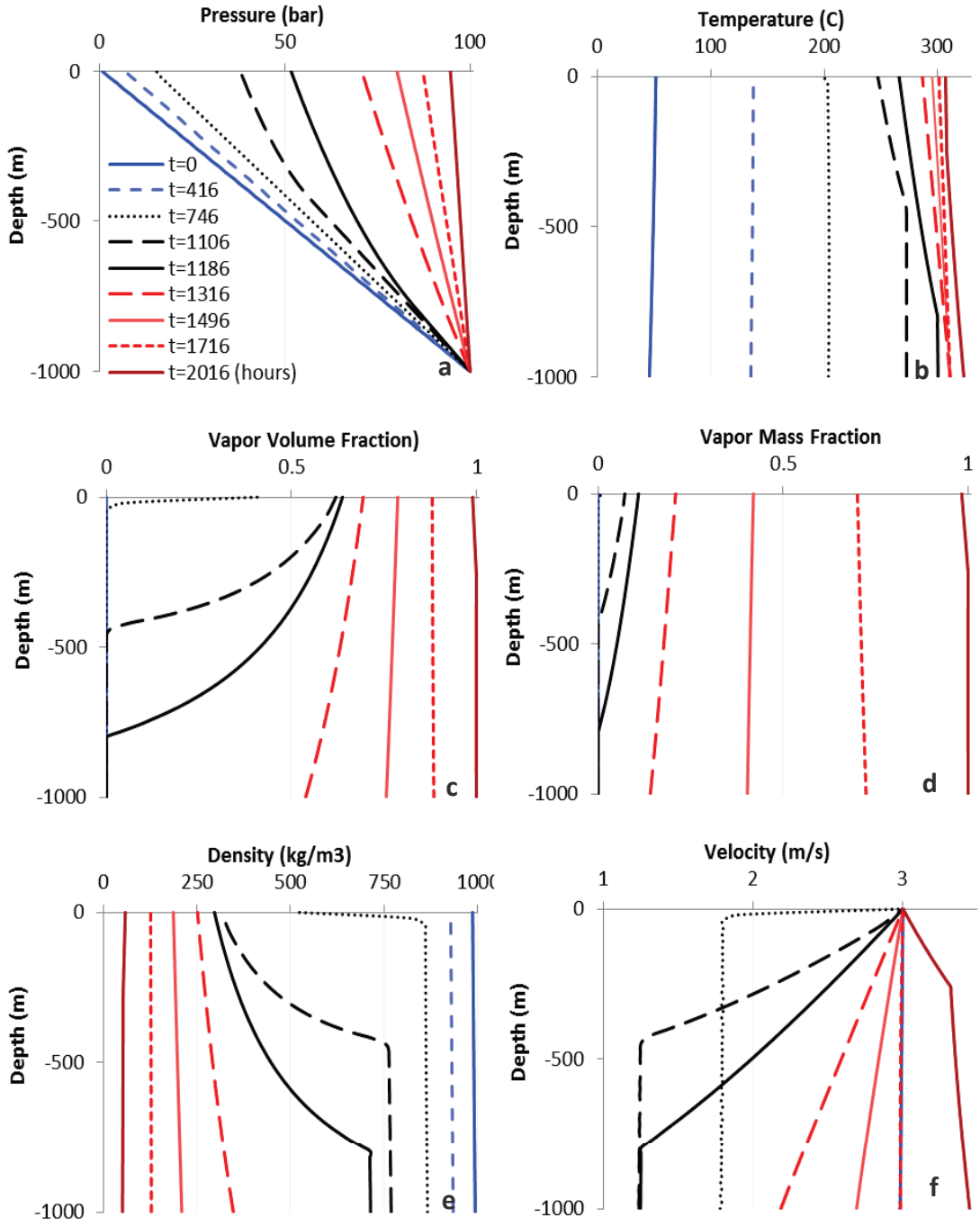

Figure 3: Pressure, temperature, vapor volume fraction, vapor mass fraction, density, and velocity variations along the well bore for various enthalpy boundary conditions.

4.2 Experimental validation

The objective of this numerical example is to validate the computational results against field experimental data obtained from a high enthalpy geothermal reservoir.

The Sabalan geothermal system, northwest of Iran, is a geothermal reservoir with high-temperature and relatively low pressure. The temperature of Sabalan reservoir is below boiling point, suggesting that it is a liquid-dominated reservoir [23]. This site contains several drilled

wellbores, but here we study the behavior of one of them, coined NWS-1. The geometrical and physical properties of the wellbore are given Table 2. The reservoir starts from depth 800 m, and the length of wellbore production part is 1570 m, as shown in Figure 4.

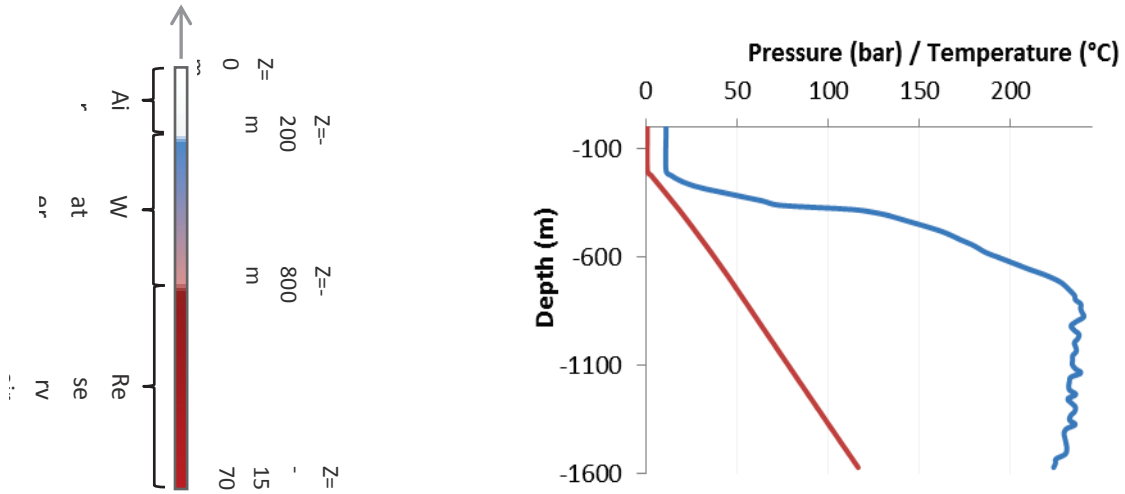

Figure 4: Down hole measured stable temperature (Blue log) and pressure (red log) along the NWS-1 wellbore; The top 200 meter of well has been filled with air in the natural state.

Table 2: Geometry and properties of NWS-1 Sabalan

Inclination Angle	90
Well head elevation	2630 (m)
Well inner radius (r_i)	0.12224 (m)
Casing outer radius (r_o)	0.14224 (m)
Production Part length (L)	1570 (m)
Reservoir depth	800 (m)
Casing thermal conductivity (λ_p)	0.16 ($Wm^{-1}K^{-1}$)
Roughness of the wellbore (ε)	1.5E-6 (m)
Surface temperature $(T_{surface})$	11 ℃
Natural Wellhead pressure (WHP)	0.75 (*bar*)
The max. flowing WHP	4.5 (*bar*)
Maximum Measured temperature	240 ℃
Profile parameter (C0) & Drift flux velocity (u_{gu})	Eq. (A 8)

Initially, the wellbore is filled with water from the well bottom at 1570 m depth to 200 m below the well head, where above this level, the wellbore is filled with air. The measured temperature log along the wellbore and in the reservoir is shown in Figure 4. At the surface, the temperature is on average 11 C and remains nearly the same until 200 m below the surface, due to the presence of air and its contact with the atmosphere. Below this level, the temperature increases until reaching around 240 C at 800 m below the surface. The figure also shows the measured pressure distribution along the wellbore, where in the top 200 m the

pressure is atmospheric at 0.77 bar, and below this level, the pressure increases hydrostatically to reach to around 117 bar at the bottom hole.

As the reservoir pressure is not high enough to generate buoyancy forces that can lift the reservoir water to the ground surface, the NWS-1 wellbore was partly filled with water, and partly with air. To facilitate discharge from the well, the airlifting technology was conducted [24]. Airlift is a technology, which aims at reducing the mass density of the initial liquid inside the wellbore by injecting air that leads the newly formed water-dry air mixture to be less dense [25].

During airlifting, it is reasonable to assume that the mass density of the newly mixed water-dry air fluid, ρ_{wa}, is homogeneous along the wellbore. Knowing the initial hydrostatic bottom hole pressure, 117 bar, and the height of the wellbore, 1570 m, the average mass density of the mixture can then be readily calculated as 758 kg/m3, equivalent to a mixture of 12.7% air and 87.3% water. This assumption of having a homogeneous mass density along the wellbore is of no significance to the transient computational results during production, but essential to establish the initial condition.

- **Initial and Boundary conditions**

Initially, the pressure and temperature along the wellbore, obtained from the field measurements, are given in Figure 4. The mass density of the water mixture is, as stated above, 758 kg/m3. The specific enthalpy is calculated based on the measured pressure and temperature, using Eq. (9).

Figure 6 shows the initial mixture properties along the wellbore. All other properties including velocity, vapor volume and vapor mass fraction are set initially to zero.

The boundary conditions at the wellhead and well bottom, using Eq. (21) and (22) , are:

Wellhead, z = 0 m:

$$\Gamma_{WHD}:\ \hat{u}_m = \frac{\hat{q}(t, z=0)}{A\rho} \qquad (\mathrm{ms}^{-1}) \tag{30}$$

Well bottom, z = -1570 m:

$$\Gamma_{bottom}: \hat{P} = \begin{cases} 11.7 & t < 72000\ s \\ \int_{-1570}^{0} \rho g\, dz + \frac{\rho u}{4 r_i} \int_{-1570}^{0} f u\, dz + \hat{P}(t, z=0) & t \geq 72000\ s \end{cases} \quad (\mathrm{MPa}) \tag{31}$$

$$\hat{h}_m = h_l\left(\hat{T}, \hat{P}\right)(J\ kg^{-1}) \quad \text{for} \quad \hat{T} = 225\ (^{\circ}\mathrm{C})$$

where $\hat{T} = 225\ (^{\circ}\mathrm{C})$ and $\hat{P} = 11.7\ (MPa)$ are obtained from the measured initial condition, given in Figure 4 ,and h_l is calculated from Eq. (9). "$\hat{q}(t, z=0)$" and "$\hat{P}(t, z=0)$" define the fluid flow rate and pressure at the wellhead, respectively. According to the field data, the maximum wellhead pressure, at which the wellbore could sustain during production, was 4.5

bar; and the mass flow rate was 30 kg/s at 3.4 bar, and 20 kg/s at 4 bar wellhead pressure. The variations of the wellhead pressure and mass flow rate with time are shown in Figure 5.

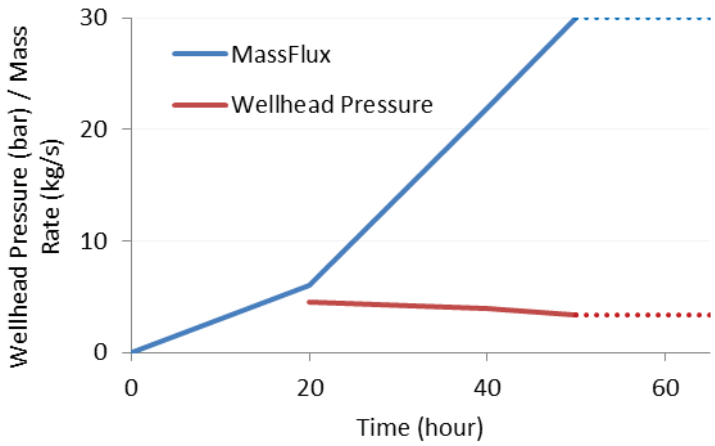

Figure 5: Wellhead pressure and mass flow rate boundary conditions

4.2.1 Finite element calculation

Using COMSOL, the wellbore is spatially discretized using 78 linear elements, and temporally, the time is discretized using the backward differentiation formula (BDF).

The finite element calculation is conducted in two overlapping steps. In the first step, two fluids flow is modeled to simulate the airlifting and the start of pumping from the reservoir. In this step, there exist two fluids exhibiting a jump in thermodynamic properties at the boundary between them. In the second step, one fluid mixture is modeled to simulate the flow of the reservoir liquid water-vapor mixture. This process starts upon the end of the airlifting process and the reach of the reservoir fluid to the wellbore head.

4.2.2 Modeling airlifting

Upon airlifting and start of production, the two mixtures; water-dry air (in the wellbore), and water-vapor (from the reservoir); travel simultaneously along the wellbore. At the interface between the two mixtures, the velocity and pressure are continuous, but the mass density and enthalpy exhibit discontinuity. In finite element analysis, the presence of a discontinuity in the physical field often causes numerical oscillations. To tackle this problem, we utilize the Level-Set (LS) method.

The LS method is a numerical technique usually utilized to trace a moving interface between two fluids. Olsson and Kreiss [26] proposed a level set formulation based on a smoothed Heaviside function, described as

$$\emptyset = H(\emptyset_d) = \begin{cases} 0 & \emptyset_d < -\varepsilon \\ \frac{1}{2} + \frac{\emptyset_d}{2\varepsilon} + \frac{1}{2\pi}\sin\left(\frac{\pi\emptyset_d}{\varepsilon}\right) & -\varepsilon \le \emptyset_d \le \varepsilon \\ 1 & \emptyset_d > \varepsilon \end{cases} \quad (32)$$

where $\emptyset_d = \min\left(\left|z - z_{\Gamma_d}\right|\right)$ and ε is a transition zone between 0 and 1. The interface between the two mixtures, Γ_d, is located at $\emptyset = 0.5$, such that: $\Gamma_d = \{z|\emptyset(z,t) = 0.5\}$. $\emptyset = 0$ indicates water-vapor mixture, and $\emptyset = 1$ indicates water-dry air mixture.

The LS function is advected by a field motion equation of the form:

$$\frac{\partial \emptyset}{\partial t} + u \,.\nabla\emptyset = \gamma_{ls}\nabla.\left(\varepsilon\nabla\emptyset - \varphi(1-\emptyset)\frac{\nabla\emptyset}{|\nabla\emptyset|}\right) \quad (33)$$

where u is the drift-flux fluid velocity, and γ_{ls} is a stabilization parameter, chosen here as 0.0001 by trail and error. According to Owkes and Desjardins (2013), if γ_{ls} is too small, $\emptyset$ exhibits oscillations, and if γ_{ls} is too large, the front advects incorrectly. ε depnds on the element size, and chosen to be as small as possible to avoid excessive mass conservation errors, while maintaining reasonable resolution of the level set function to avoid numerical difficulties [15].

Having located $\emptyset$, the mass density and specific heat capacity, are calculated as

$$\rho = \rho_m + (\rho_{wa} - \rho_m).\emptyset \quad (34)$$

and

$$C_p = C_{p_m} + \left(C_{p_{wa}} - C_{p_m}\right).\emptyset \quad (35)$$

in which the subscript m indicates formation water-vapor mixture and subscript wa indicates the airlifted water-dry air mixture. The jump in the material thermal conductivity, viscosity, and temperature are treated in the same way.

4.2.3 Modeling energy production

The production process starts from the end of the airlifting until t = 100 hours. During this period, only the reservoir water liquid-vapor mixture exists along the wellbore. The level set function in this step is zero.

4.2.4 Finite element results and discussion

Figure 6 shows the computed mixture parameter distributions along the wellbore during airlifting and production.

Figure 6a shows the level set distribution during the airlifting. Initially, before the start of production, the level set distance parameter reads $\emptyset = 1$, indicating that the wellbore is filled with the initial liquid water-dry air fluid, shown in all figures of the Figure 6 by the small dotted blue line. At the end of airlifting, the level set parameter reads $\emptyset = 0$, indicating that the wellbore is filled with the reservoir water liquid-vapor fluid, shown in the figure by the solid red line. For $0 < \emptyset < 1$, the level set parameter denotes the location of the interface between the two fluids along the wellbore. The figure shows a smooth transition between the two mixtures, as prescribed by Eq. (34). The air lifting process takes 10 hours, after which the reservoir water reaches to the well head.

Figure 6b, shows the pressure distribution along the wellbore. The dotted blue lines show the

pressure distribution during the airlifting. The figure shows that, at the beginning, the bottom hole pressure is fixed at 117 bars, prescribed in Eq. (31), and the reduction along the wellbore is hydrostatic. After 20 hours of production, the pressure at the bottom hole becomes a function of the wellhead pressure, friction and hydrostatic pressure, which is significantly affected by the increase in vapor content.

The increase in vapor volume and mass fractions are shown in Figure 6c and 7d. These figures show a significant increase in the vapor contents at the flash evaporation locations along the wellbore. The flash evaporation occurs due to reduction of pressure, accompanied by a certain range of high temperature.

Figure 6e shows the temperature distribution along the wellbore. The temperature at the bottom is 225℃, assumed equal to the reservoir temperature. The well head temperature varies from initially 11 ℃ to about 140 ℃ after 50 hours of production and stays constant till 100 hours. The temperature log shows the flash points, where there is a sharp decrease in temperature in the downstream as compare to that at the upstream, due latent heat vaporization. The locations of these flash points are consistent in all other property distributions.

Figure 6f shows the specific enthalpy distribution along the wellbore. With increasing the mass flow rate, the specific enthalpy exhibits little variation. For a 30 kg/s flow rate, the computed wellhead specific enthalpy is 965 ($kJ\ kg^{-1}$), similar to that at the bottom hole. The bottom hole enthalpy is computed as a function of the bottom hole pressure and temperature, using Eq. (31), but yet it can be assumed constant because the variation is too small, ranging between 969 and 967 ($kJ\ kg^{-1}$).

Figure 6g shows the distribution of mass density along the wellbore. As expected, the mixture density starts to drop at the flash point, in contrary to the vapor content. After 50 hours of production, it reaches to a minimum value of 110 kg/m3 at the wellhead, related to about 88% vapor volume fraction.

Figure 6h shows the velocity distribution along the wellbore. The increase of velocity with time is in consistence with the increase of the flow rate, given in Figure 5. The figure shows that, at the flash points, the velocity exhibits a sharp increase.

At the end of production, after 100 hours, the vapor volume fraction at the wellhead is 0.88 and the mass fraction is 0.18. The wellhead pressure is 3.4 bar, related to the maximum flow rate of 30 kg/s. these information could be efficiently used for separator designing and power generating.

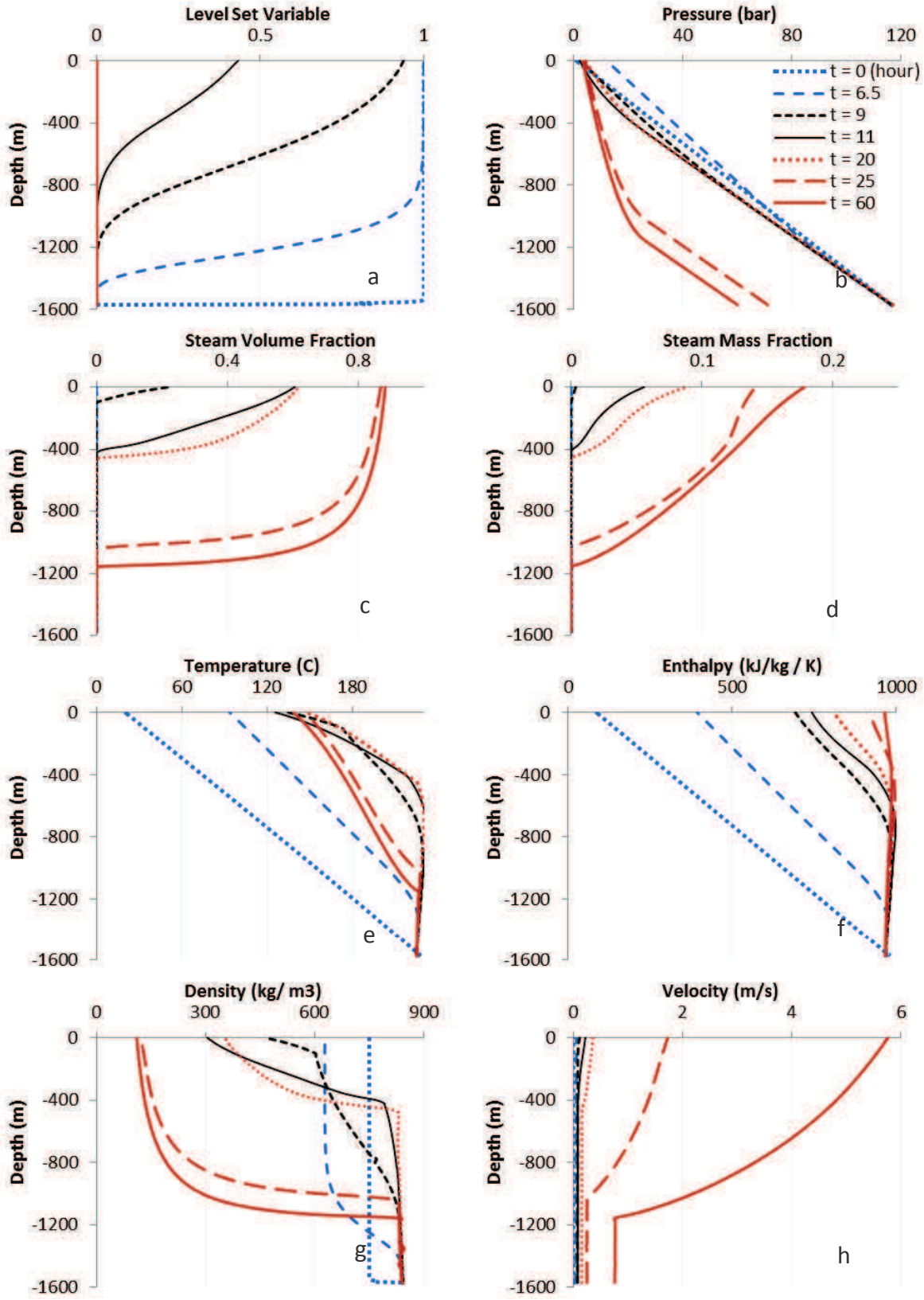

Figure 6: simulated properties of fluid during the flowing time along the wellbore

4.2.5 Comparison to measured data

The computational results are compared to the available measured data from the field, taken at the wellhead and along the wellbore. Figure 7 shows the computed and measured pressure and temperature distributions for the maximum flow rate of 30 kg/s, at t = 100 hours. Table 3 and Table 4 show detailed comparison at the wellhead and along the wellbore.

Apparently, there is a good agreement between the computed results and the measured data. However, the computed temperature at the wellhead is 139 C, while the measured one is 150 C. This can be attributed to the changes in the surface air temperature, which, in the model, considered constant. The computed flashing depth is 1136 m, while the measured is around 1170 m. Even though this difference is not significant compared to the wellbore length, the difference can be attributed to that not all initial and boundary conditions are measured, and in the model we ought to back calculate them to infer the field conditions, which most likely not exact.

Table 3: Simulation results versus measured data at the wellhead

	Pressure (bar)	Total flow rate (kg/s)	Steam mass rate (kg/s)	Enthalpy (kJ/kg/K)
Measured	4.00	22	3.68	950 - 1000
Simulated	Prescribed BC	Prescribed BC	3.61	956.88
Measured	3.4	30	5.5	950 - 1000
Simulated	Prescribed BC	Prescribed BC	5.4	965

Table 4: Simulation results versus measured data along the wellbore

	Bottom hole flowing Pressure (bar)	Flashing depth (m)	Wellhead temperature (C)	Flashing point temperature (C)
Measured	60.09	1170	150	223
Simulated	60.17	1136	139	223

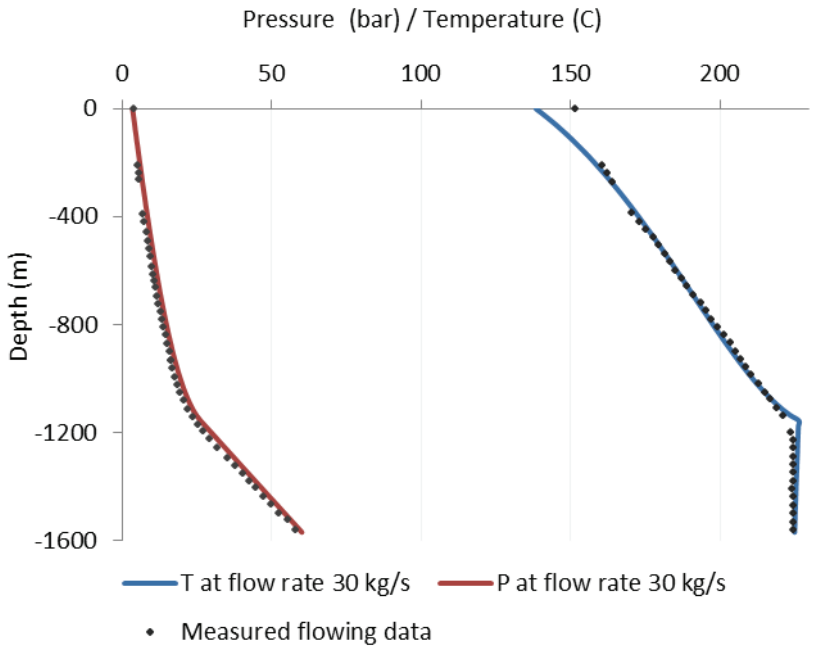

Figure 7: Simulation results versus measured data along the wellbore

4.3 Parametric analysis

Three parametric analyses have been conducted to study the effects of: (i) wellbore diameter, (ii) wellbore wall roughness, and (iii) drift flux profile parameter. The first two parameters are physical, and normally utilized for wellbore design, and the third is numerical, and employed for the evaluation of the drift flux constitutive models. The geometry and material parameters, except for the examined parameters, utilized in this analysis are similar to those adopted in the numerical example given in Section 4.2 .

1. **Wellbore diameter**: Three wellbore diameters are examined: 16.4 cm, 24.4 cm and 32.4 cm. Figure 9shows the computational results of pressure, temperature, void fraction and steam mass fraction distributions along the wellbore for the three cases. It illustrates that by increasing the wellbore diameter from 16.4 cm to 24.4 cm, the flashing zone depth moves from 970 m to 1170 m, and at the wellbore bottom-hole, the pressure decreased from 75 bar to 60 bar. However, the increase of the wellbore diameter from 24.4 cm to 32.4 cm exhibits no significant effect. The void fractions, steam fraction, pressure and temperature at the wellhead are nearly the same for the three cases.
2. **Wellbore wall roughness**: Three friction coefficients are examined: 0.015 mm, 0.0015 mm and 0.00015 mm. Figure 9 shows the computational results of pressure, temperature, void fraction and steam mass fraction distributions along the wellbore for the three cases. It illustrates that, for the studied cases, the wellbore wall roughness has no significant effect on the fluid flow.
3. **Drift flux profile parameter**: Three constitutive equations, Eqs. A6, A7 and A8 given in Table A1, describing the drift flux profile parameter, C_0, and its associated drift flux velocity, u_{gu}, are examined. Figure 10 shows the computational results of pressure, temperature, void

fraction and steam mass fraction distributions along the wellbore for the three cases. It demonstrates that Eq. A6 and Eq. A8 produce reasonably similar computational results along the wellbore, but Eq. A7 exhibits deviation from both, though with similar trend. Following our verification example given in Section 4.2, it seems that Eq. A8 has produced the best fit, followed by Eq. A6.

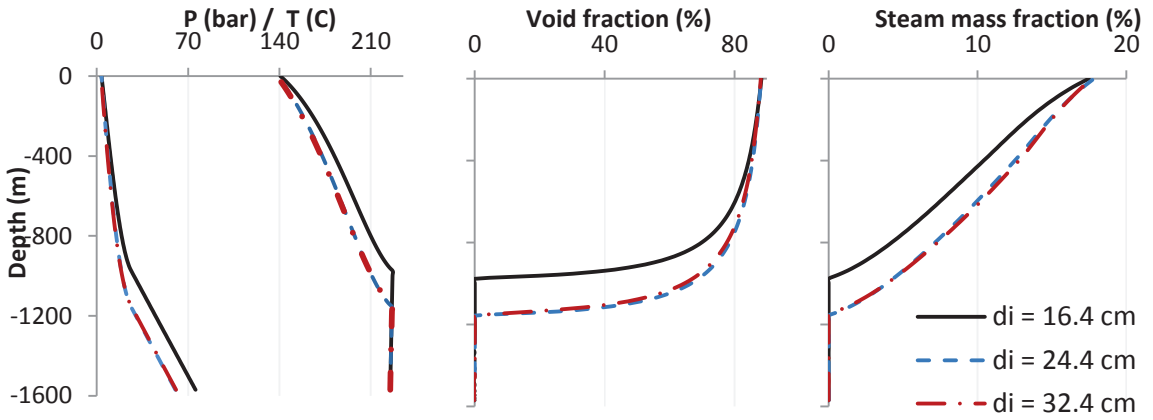

Figure 8: Effect of well diameter, at t = 60 hour

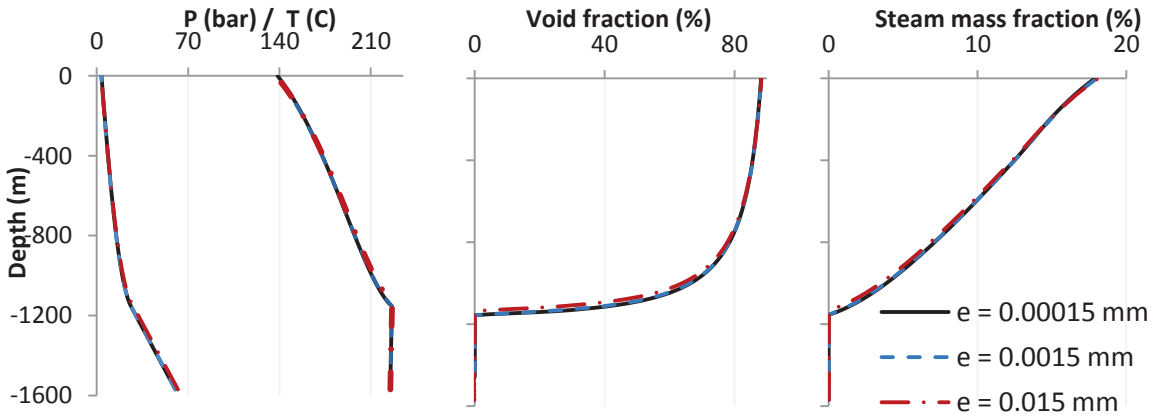

Figure 9: Effect of wellbore roughness, at t = 60 hour

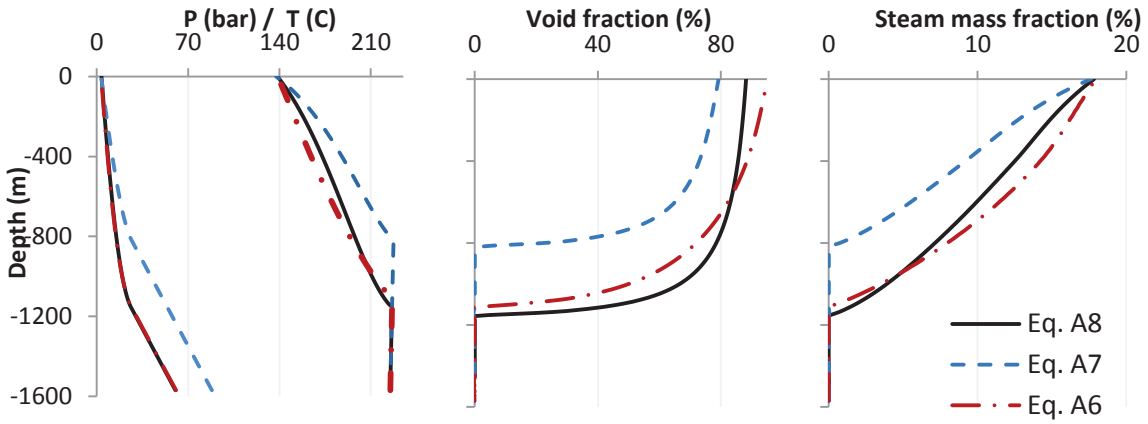

Figure 10: Effect of different constitutive models for the drift flux profile parameter, at t = 60 hour

5 Conclusion

In high enthalpy geothermal systems, predicting the fluid properties along the wellbore, such as temperature, phase composition and mass density is vital for their design and monitoring. The fluid along the wellbore exhibits phase change, which is manifested by the occurrence of flash evaporation, arising from pressure reduction, accompanied by a certain range of temperatures. Below and above the flash point, the fluid exhibits sudden change in material composition, which can cause a significant change in its properties and behavior. Such kind of physical behavior is computationally challenging and demanding. Solving this kind of problems constitutes the focal point of the presented work.

The conceptual model and the mathematical formulation are designed to simulate a wide range of enthalpies and initial and boundary conditions. All important physical phenomena and processes occurring along the wellbore, including buoyancy, phase change, compressibility, thermal interaction, wall friction and slip between phases are considered. They are also designed to simulate airlifting of water and air, which initially exist in the wellbore before production. The airlifting inevitably gives rise to the existence of two fluids along the wellbore: airlifted water-dry air fluid, and reservoir water-vapor fluid. At the boundary between the two fluids there is a discontinuity in the thermodynamic properties. The discontinuity is modeled using the level-set method, which is coupled to the drift-flux model via the fluid velocity.

The numerical model is designed to solve the governing equations using the finite element method. The finite element package, COMSOL Multiphysics, is utilized as a framework for implementing and discretizing the governing equations. These equations are dynamic, advective, nonlinear and involve phase change, together with buoyancy, friction, slip forces and discontinuity at the boundary between two fluids. Solving such a problem using standard strong form implementation is not possible, unless excessively fine meshes and small time steps are utilized. Yet, the calculation can be unstable and non-convergent. Instead, we solved this problem by implementing the weak forms of the governing equations, using the weighted

residual finite element method.

The computational capability of the model has been tested by solving two numerical examples with different initial and boundary conditions. The computational results clearly exhibit the occurrence of phase change along the wellbore, the extent of which depends on the enthalpy of the reservoir. The accuracy of the model is examined by comparing its results with those obtained from field data.

The parametric analyses have shown that the model can be readily utilized for engineering design of geothermal wellbores. We show that the increase of wellbore diameter can change the fluid state profile along the wellbore, but to a certain limit, after which, the increase of diameter will not have a significant effect. We also show that the wall roughness has, for the studied range, no significant effect.

The paper shows that, despite the complexity of the involved physical phenomena, it is possible to model such a problem using commercial packages, supporting user programing interface, as a framework for discretization. However, an innovative implementation of the governing equations is necessary, and requires an in depth knowledge on the mathematical formulation, numerical discretization and software features.

Appendix A. Model Parameters

The wellbore wall friction coefficient, f, in Eq. (2), can be described as [11]:

$$f = \begin{cases} \dfrac{16}{\mathrm{Re}} & Re \le 2400 \\ \dfrac{1}{16}\left\{\log\left[\dfrac{\xi}{3.7r_i} - \dfrac{5.02}{Re}\log\left(\dfrac{\xi}{3.7r_i} + \dfrac{13}{Re}\right)\right]\right\}^{-2} & Re \ge 2400 \end{cases} \quad \text{(A 1)}$$

where ξ is the roughness of the wellbore, assumed 0.0015 mm, and Re is the Reynolds number given by:

$$\mathrm{Re} = \frac{\rho_m |u_m| (2r_i)}{\mu_m} \quad \text{(A 2)}$$

in which μ_m is the dynamic viscosity, described in Eq. (A 12).

The slip parameter between two phases , γ, in the momentum balance equation, could be defined as [12]:

$$\gamma = \frac{\alpha \rho_g \rho_l \rho_m}{(1-\alpha)\,{\rho_m^*}^2}\left[(C_0 - 1)u_m + u_{gu}\right]^2 \quad \text{(A 3)}$$

where α is the gas volume fraction, ρ_g is the gas density and ρ_l is the liquid density, and ρ_m^* defines the profile-adjusted average density, described as:

$$\rho_m^* = \alpha C_0 \rho_g + (1 - \alpha C_0)\rho_l \quad \text{(A 4)}$$

u_{gu} and C_0 are the drift flux velocity and profile parameter, respectively. Table A 1 gives

various definitions, with their corresponding literature. Here we utilize Eq. (A 7) and (A 8) in example 1 and 2, respectively.

σ_{gl} is the surface tension, valid over the vapor-liquid saturation line for the temperature range between 0 and 373.946 ℃ [21]. It is described as

$$\sigma_{gl} = 0.2358(1 - \frac{T}{647.096})^{1.256}\left[1 - 0.625(1 - \frac{T}{647.096})\right] \quad \text{(A 5)}$$

Table A 1: Various expressions for C0 and $\mathbf{u_d}$

Expression	Eq. Number	Reference
$$C_0 = \frac{C_{max}}{1 + (C_{max} - 1)\eta^2}$$ $$\eta = \frac{\beta - B}{1 - B}$$ $$B = \frac{2}{C_{max}} - 1.0667$$ $$\beta = \max\left(\alpha_2, F_V \frac{\alpha_2 \lvert u_m \rvert}{u_{sgf}}\right), 0 \le \beta \le 1$$ $$u_{sgf} = K_u \left(\frac{\rho_1}{\rho_2}\right)^{0.5}\left[\frac{g\sigma_{gl}(\rho_l - \rho_g)}{{\rho_l}^2}\right]^{1/4}$$ $$K_u = \left[\frac{142}{\sqrt{N_B}}\left(\sqrt{1 + \frac{N_B}{161.312}} - 1\right)\right]^{0.5}$$ $$N_B = 4{r_i}^2\left[\frac{g(\rho_l - \rho_g)}{\sigma_{gl}}\right]$$ where C_{max} is assumed 1.1, η is a parameter reflecting the effect of the flow status on the profile parameter, $F_V = 1$, K_u is the Kutateladze number, and N_B is the Bond number.	(A 6)	[11, 13]
$$u_{gu} = \frac{1.85(1 - \alpha C_0)K\left[\frac{g\sigma_{gl}(\rho_l - \rho_g)}{{\rho_l}^2}\right]^{1/4}}{\alpha C_0\sqrt{\frac{\rho_g}{\rho_l}} + 1 - \alpha C_0}$$ for a vertical wellbore K is a smooth transition function defined as: $$K = \begin{cases} 1.53 & \alpha \le 0.06 \\ 1.53 + \frac{C_0 K_u - 1.53}{2}\left[1 - cos\,(\pi \frac{\alpha - 0.06}{0.15})\right] & 0.06 \le \alpha \le 0.21 \\ C_0 K_u & \alpha \ge 0.21 \end{cases}$$		

$C_0 = 1 + 0.2(1-X)\left(\frac{g d_i {\rho_l}^2}{m^2}\right)^{0.25}$ for $\alpha \geq 0.1$ m is the mass velocity. $C_0 = 1 + 0.2(1-X)$ for $\alpha < 0.1$	$u_{gu} = 1.18\,(1-X)\left[\frac{g\sigma_{gl}(\rho_l - \rho_g)}{{\rho_l}^2}\right]^{1/4}$	(A 7)	[19, 20]
$C_0 = 1.1$ for $m \geq 200$ $C_0 = 1.54$ for $m < 200$ m is the mass velocity	$u_{gu} = 1.18\left[\frac{g\sigma_{gl}(\rho_l - \rho_g)}{{\rho_l}^2}\right]^{1/4}$	(A 8)	[19, 20]
$C_0 = 1.2$	$u_{gu} = 1.53\left[\frac{g\sigma_{gl}(\rho_l - \rho_g)}{{\rho_l}^2}\right]^{1/4}$	(A 9)	[2]

Q in Eq. (3) describes the heat exchange between the wellbore wall and its surrounding formation, defined as [11]:

$$Q(z) = 2\pi r_w U(T - T_R(z)) \quad \text{(A 10)}$$

$$U = \frac{1}{R_{conv} + R_{cond}}$$

$$R_{conv} = r_0/(r_w \bar{h})$$

$$R_{cond} = r_0 \ln(r_0/r_w)/\lambda_p$$

$$\bar{h} = \mathrm{Nu}\,\lambda_m/(2r_i)$$

$$\mathrm{Nu} = \begin{cases} 0.665\,Re^{1/2}\mathrm{Pr}^{1/3}, & Re < 2000 \\ 0.023 Re^{0.8}\mathrm{Pr}^{0.4}, & Re \geq 2000 \end{cases}$$

$$\mathrm{Pr} = \frac{\mu_m c_{pm}}{\lambda_m}$$

where $T_R(z)$ is the temperature of the surrounding formation, in contact with the formation, and U is the thermal interaction coefficient of wellbore, with R_{conv} and R_{cond} are the thermal resistance of the fluid and casing material, respectively. r_w is the outer radius of the casing, r_0 is the outer radius of the wellbore, λ_p is the thermal conductivity of the casing material, and $\bar{h}$ is the convective heat transfer coefficient, with Nu the Nusselt number and Pr the Prandtl number. c_{pm}, μ_m and λ_m are the specific heat capacity, dynamic viscosity and thermal conductivity of the mixture described in Eqs.(A 11), (A 12) and (A 13), respectively.

The specific isobaric heat capacity is defined in terms the specific heat capacity of the liquid phase and the gas phase, and their volume fractions, as

$$C_{p_m}(P,T) = -\alpha\left(\frac{\partial h_g}{\partial T}\right)_P - (1-\alpha)\left(\frac{\partial h_l}{\partial T}\right)_P \quad \text{(A 11)}$$

in which h_g and h_l are specific enthalpies of vapor and liquid phases, described in Eqs. (9) and (

588 10), respectively.
589 Considering the effects of density and temperature, the dynamic viscosity, μ_m, and the mixture
590 thermal conductivity, λ_m, can be described as

$$\mu_m(\rho,T) = 10^{-6}\left(\frac{T}{647.096}\right)^{0.5}\left[\sum_{i=1}^{4} n_i^o\left(\frac{T}{647.096}\right)^{1-i}\right]^{-1} exp\left[\sigma_{gl}\sum_{i=1}^{21} n_i\left(\frac{\rho_m}{322} - 1\right)^{I_i}\left(\left(\frac{T}{647.096}\right)^{-1} - 1\right)^{J_i}\right] \quad \textbf{(A 12)}$$

591

$$\lambda_m(\rho,T) = \left(\frac{T}{647.26}\right)^{0.5}\sum_{i=1}^{4} n_i^o\left(\frac{T}{647.26}\right)^{i-1} + n_1 + n_2\frac{\rho_m}{317.17} + n_3 exp\left[n_4\left(\frac{\rho_m}{317.17} + n_5\right)^2\right] + \left(n_1\left(\frac{T}{647.26}\right)^{-10} + n_2\right)\left(\frac{\rho_m}{317.17}\right)^{1.8} exp\left[n_3\left(1 - \left(\frac{\rho_m}{317.17}\right)^{2.8}\right)\right] + n_4 A\left(\frac{\rho_m}{317.17}\right)^{B} \exp\left[\left(\frac{B}{1+B}\right)\left(1 - \left(\frac{\rho_m}{317.17}\right)^{1+B}\right)\right] \quad \textbf{(A 13)}$$

where

$$A = 2 + n_8\left(\left|\frac{T}{647.26} - 1\right| + n_{10}\right)^{-0.6}$$

$$B = n_9\left(\left|\frac{T}{647.26} - 1\right| + n_{10}\right)^{-0.6} \quad for \quad T < 647.26$$

592 where the n_i coefficients are constant values, which can be found in IAPWS-IF97.

593 **Appendix B. IAPWS formulation of water and steam**

594 The temperatures of geothermal resources for most known fields range from about 50 ℃, in
595 low enthalpy fields, to about 160 – 280 ℃, in relatively high enthalpy fields. According to Figure
596 1, this range of temperatures is included in regions 1, 2 and 4, which are related to liquid, gas
597 and two-phase mixture, respectively.
598 The specific Gibbs free energy, g_1 and g_2, for single-phase fluid, which falls in region 1 or 2 can
599 be described respectively as

$$g_1(P,T) = R\,T\sum_{i=1}^{34} n_i\left(7.1 - \frac{P}{16.53E6}\right)^{I_i}\left(\frac{1386}{T} - 1.222\right)^{J_i} \quad \textbf{(B 1)}$$

$$g_2(P,T) = R\,T \ln\left(\frac{P}{1\text{E}6}\right)\sum_{i=1}^{9} {n_i}^o \left(\frac{540}{T}\right)^{{J_i}^o} + R\,T\sum_{i=1}^{43} n_i \left(\frac{P}{1\text{E}6}\right)^{I_i}\left(\frac{540}{T}-0.5\right)^{J_i} \quad \textbf{(B 2)}$$

where $\mathrm{R} = 461.526\ \mathrm{J}kg^{-1}K^{-1}$.

For a vapor mass fraction of more than 95%, $g_2(P,T)$ is replaced by what is known as the metastable vapor equation, which is only different from Eq. (B 2) by its coefficients [21]. For region 4, however, the saturation liquid properties are calculated by Eqs. (B 1) of region 1, and the saturation vapor properties are calculated by Eqs. (B 2) of region 2.

The coefficient $n_i, {n_i}^o, {n_i}', I_i, J_i, {J_i}^o$ can be found in IAPWS-IF97 [21]. They have different values in different equations.

References

1. Poettmann, F.H. and P.G. Carpenter, *Multiphase Flow of Gas, Oil and Water through Vertical Strings with Application to the Design of Gas Lift Installation*, in *API (American Petroleum Institute) Drilling and Production Practice*. 1952: Midland. Texas. p. 257-317.
2. Zuber, N. and J.A. Findlay, *Average Volumetric Concentration in Two-Phase Flow Systems.* Journal of Heat Transfer, 1965. **87**: p. 453-468.
3. Gould, T.L., *Vertical Two-Phase Steam-Water Flow in Geothermal Wells.* Journal of Petroleum Technology, 1974. **26**: p. 833-842.
4. Goyal, K.P., C.W. Miller , and M.J. Lippmann. *Effect of Wellhead Parameters and Well Scaling on the Computed Downhole Conditions in Cerro Prieto Wells*. in *The 6th Workshop on Geothermal Reservoir Engineering* 1980. Stanford University, Stanford, California, USA.
5. Miller, C.W., *Welbore User's Manual*. 1980, Berkeley, University of California.
6. Aunzo, Z.P., G. Bjornsson, and G.S. Bodvarsson, *Wellbore Models GWELL, GWNACL, and HOLA User's Guide*. 1991: Berkeley, University of California, USA
7. Bjornsson, G. and G.S. Bodvarsson, *A Multi-feed zone geothermal wellbore simulator. .* Geothermal Resources Council Transactions, 1987. **11**: p. 503–507.
8. Gudmundsdottir, H., M. Thor Jonsson, and H. Palsson. *THE WELLBORE SIMULATOR FLOWELL*. in *Thirty-Eighth Workshop on Geothermal Reservoir Engineering*. 2013. Stanford University, Stanford, California.
9. Saeid, S., R. Al-Khoury, and F. Barends, *An efficient computational model for deep low-enthalpy geothermal systems.* Computers & Geosciences, 2013. **51**: p. 400-409.
10. Kaya, A.S., C. Sarica, and J.P. Brill. *Comprehensive Mechanistic Modeling of Two-Phase Flow in Deviated Wells*. in *Society of Petroleum Engineers Annual Technical Conference*. 1999. Houston, Texas.
11. Mousivand Arzanfudi, M. and R. Al-Khoury, *A compressible two-fluid multiphase model for CO2 leakage through a wellbore.* International Journal for Numerical Methods in Fluids, 2015. **77**(8): p. 477–507.

12. Pan, L.H., S.W. Webb, and C.M. Oldenburg, *Analytical solution for two-phase flow in a wellbore using the drift-flux model.* Advances in Water Resources, 2011. **34**(12): p. 1656-1665.
13. Shi, H., Holmes, J. A., Durlofsky, L. J., Aziz, K., Diaz, L., Alkaya, B., & Oddie, G. , *Drift-Flux Modeling of Two-Phase Flow in Wellbores.* Society of Petroleum Engineers, 2005.
14. Faghri, A. and Y. Zhang, *Transport Phenomena in Multiphase Systems*. 2006, USA: Elsevier.
15. Owkes, M. and O. Desjardins, *A discontinuous Galerkin conservative level set scheme for interface capturing in multiphase flows.* Journal of Computational Physics, 2013. **249**: p. 275-302.
16. Sethian, J.A. and P. Smereka, *Level Set Methods for Fluid Interfaces.* Annual Review of Fluid Mechanics, 2003. **35**(35): p. 341-372.
17. Lewis, K.C. and R.P. Lowell, *Numerical modelling of two-phase flow in NaCl-H2O flow in the NaCl-H2Osystem: Introduction of a numerical method and benchmarking.* Journal of Geophysical research, 2009. **114**: p. 1-18.
18. Palliser, C.C. and R. McKibbin, *A Model for Deep Geothermal Brines,III: Thermodynamic Properties – Enthalpy and Viscosity.* Transport in Porous Media 1998. **33**(1): p. 155-171.
19. Rouhani, S. and E. Axelsson, *Calculation of Void Volume Fraction in the Subcooled and Quality Boiling Regions.* Journal of Heat and Mass Transfer, 1970. **13**(2): p. 383-393.
20. Thome, j.r., *Chapter 17:Void fraction in two phase flows*, in *engineering data book III*. 2004, Wolverine Tube, Inc.
21. Wagner, W. and H.J. Kretzschmar, *International Steam Tables - Properties of Water and Steam Based on the Industrial Formulation IAPWS-IF97*. 2008: Springer-Verlag (Berlin).
22. Süli, E. and D. Mayers, *An Introduction to Numerical Analysis*. 2003: Cambridge University Press.
23. Porkhial, S., et al. *Interpretation of the Injection and Heat Up tests at Sabalan geothermal field, Iran*. in *World Geothermal Congress 2015*. 2015. Melbourne, Australia.
24. Rahmani, M.R., *Assesment of calcite scaling potential in the geothermal wells of the NW-Sabalan geothermal prospect, NW-Iran*. 2007, GEOTHERMAL TRAINING PROGRAMME, Iceland: report for SUNA (Renewable Energy Organization of Iran).
25. Grant, M.A. and P.F. Bixley, *Chapter 8: Production Testing*, in *Geothermal Reservoir Engineering*. 2011, Elsevier Inc.
26. Olsson, E. and G. Kreiss, *A conservative level set method for two phase flow.* Journal of Computational Physics, 2005. **210**: p. 225-246.

Revised Table

Table 1: Wellbore and formation assumed data

Inclination Angle	90
Well inner radius (r_i)	0.11 (m)
Casing outer radius (r_o)	0.13 (m)
Length (l)	1000 (m)
Casing thermal conductivity (λ_p)	0.33 ($Wm^{-1}K^{-1}$)
Roughness of the wellbore (ε)	1.5E-6 (m)
Surface temperature $(T_{surface})$	20 ℃
Profile parameter (C0) & Drift flux velocity (u_{gu})	Eq. **Error! Reference source not found.**

Table 2: Geometry and properties of NWS-1 Sabalan

Inclination Angle	90
Well head elevation	2630 (m)
Well inner radius (r_i)	0.12224 (m)
Casing outer radius (r_o)	0.14224 (m)
Production Part lenght (L)	1570 (m)
Reservoir depth	800 (m)
Casing thermal conductivity (λ_p)	0.16 ($Wm^{-1}K^{-1}$)
Roughness of the wellbore (ε)	1.5E-6 (m)
Surface temperature $(T_{surface})$	11 ℃
Natural Wellhead pressure (WHP)	0.75 (*bar*)
The max. flowing WHP	4.5 (*bar*)
Maximum Measured temperature	240 ℃
Profile parameter (C0) & Drift flux velocity (u_{gu})	Eq. **Error! Reference source not found.**

Table 3: Simulation results versus measured data at the wellhead

	Pressure (bar)	Total flow rate (kg/s)	Steam mass rate (kg/s)	Enthalpy (kJ/kg/ K)
Measured	4.00	22	3.68	950 - 1000
Simulated	Prescribed BC	Prescribed BC	3.61	956.88
Measured	3.4	30	5.5	950 - 1000
Simulated	Prescribed BC	Prescribed BC	5.4	965

Table 4: Simulation results versus measured data along the wellbore

	Bottom hole flowing Pressure (bar)	Flashing depth (m)	Wellhead temperature (C)	Flashing point temperature (C)
Measured	60.09	1170	150	223
Simulated	60.17	1136	139	223

Table A 1: Various expressions for C0 and u_d

Expression	Eq. Number	Reference

$$C_0 = \frac{C_{max}}{1 + (C_{max} - 1)\eta^2}$$

$$\eta = \frac{\beta - B}{1 - B}$$

$$B = \frac{2}{C_{max}} - 1.0667$$

$$\beta = \max\left(\alpha_2, F_V \frac{\alpha_2 |u_m|}{u_{sgf}}\right), 0 \le \beta \le 1$$

$$u_{sgf} = K_u \left(\frac{\rho_1}{\rho_2}\right)^{0.5} \left[\frac{g\sigma_{gl}(\rho_l - \rho_g)}{{\rho_l}^2}\right]^{1/4}$$

$$K_u = \left[\frac{142}{\sqrt{N_B}}\left(\sqrt{1 + \frac{N_B}{161.312}} - 1\right)\right]^{0.5}$$

$$N_B = 4{r_i}^2 \left[\frac{g(\rho_l - \rho_g)}{\sigma_{gl}}\right]$$

where C_{max} is assumed 1.1, η is a parameter reflecting the effect of the flow status on the profile parameter, $F_V = 1$, K_u is the Kutateladze number, and N_B is the Bond number.

$$u_{gu} = \frac{1.85(1 - \alpha C_0) K \left[\frac{g\sigma_{gl}(\rho_l - \rho_g)}{{\rho_l}^2}\right]^{1/4}}{\alpha C_0 \sqrt{\frac{\rho_g}{\rho_l}} + 1 - \alpha C_0}$$ for a vertical wellbore

K is a smooth transition function defined as:

$$K = \begin{cases} 1.53 & \alpha \le 0.06 \\ 1.53 + \frac{C_0 K_u - 1.53}{2}\left[1 - cos\,(\pi \frac{\alpha - 0.06}{0.15})\right] & 0.06 \le \alpha \le 0.21 \\ C_0 K_u & \alpha \ge 0.21 \end{cases}$$

(A 1) [11, 13]

$C_0 = 1 + 0.2(1 - X)\left(\frac{g d_i {\rho_l}^2}{m^2}\right)^{0.25}$ for $\alpha \ge 0.1$ m is the mass velocity. $C_0 = 1 + 0.2(1 - X)$ for $\alpha < 0.1$	$u_{gu} = 1.18\,(1 - X)\left[\frac{g\sigma_{gl}(\rho_l - \rho_g)}{{\rho_l}^2}\right]^{1/4}$	**(A 2)**	[19, 20]
$C_0 = 1.1$ for $m \ge 200$ $C_0 = 1.54$ for $m < 200$ m is the mass velocity	$u_{gu} = 1.18\left[\frac{g\sigma_{gl}(\rho_l - \rho_g)}{{\rho_l}^2}\right]^{1/4}$	**(A 3)**	[19, 20]
$C_0 = 1.2$	$u_{gu} = 1.53\left[\frac{g\sigma_{gl}(\rho_l - \rho_g)}{{\rho_l}^2}\right]^{1/4}$	**(A 4)**	[2]